Local structures of polar wurtzites $Zn_{1-x}Mg_xO$ studied by Raman and $^{67}Zn/^{25}Mg$ NMR spectroscopies and by total neutron scattering

Young-Il Kim,[1] Sylvian Cadars,[2] Ramzy Shayib,[2] Thomas Proffen,[3]
Charles S. Feigerle,[4] Bradley F. Chmelka,[2] and Ram Seshadri[1,5]
[1]*Materials Department and Materials Research Laboratory, University of California, Santa Barbara, California 93106, USA*
[2]*Department of Chemical Engineering, University of California, Santa Barbara, California 93106, USA*
[3]*Los Alamos National Laboratory, Lujan Neutron Scattering Center, LANSCE-12, Los Alamos, New Mexico 87545, USA*
[4]*Department of Chemistry, The University of Tennessee, Knoxville, Tennessee 37996, USA and*
[5]*Department of Chemistry and Biochemistry, University of California, Santa Barbara, California 93106, USA*
(Dated: February 2, 2022)

Local compositions and structures of $Zn_{1-x}Mg_xO$ alloys have been investigated by Raman and solid-state $^{67}Zn/^{25}Mg$ nuclear magnetic resonance (NMR) spectroscopies, and by neutron pair-distribution-function (PDF) analyses. The E_2^{low} and E_2^{high} Raman modes of $Zn_{1-x}Mg_xO$ display Gaussian- and Lorentzian-type profiles, respectively. At higher Mg substitutions, both modes become broader, while their peak positions shift in opposite directions. The evolution of Raman spectra from $Zn_{1-x}Mg_xO$ solid solutions are discussed in terms of lattice deformation associated with the distinct coordination preferences of Zn and Mg. Solid-state magic-angle-spinning (MAS) NMR studies suggest that the local electronic environments of ^{67}Zn in ZnO are only weakly modified by the 15 % substitution of Mg for Zn. ^{25}Mg MAS spectra of $Zn_{0.85}Mg_{0.15}O$ show an unusual upfield shift, demonstrating the prominent shielding ability of Zn in the nearby oxidic coordination sphere. Neutron PDF analyses of $Zn_{0.875}Mg_{0.125}O$ using a $2\times2\times1$ supercell corresponding to Zn_7MgO_8 suggest that the mean local geometry of MgO_4 fragments concurs with previous density functional theory (DFT)-based structural relaxations of hexagonal wurtzite MgO. MgO_4 tetrahedra are markedly compressed along their *c*-axes and are smaller in volume than ZnO_4 units by ≈ 6 %. Mg atoms in $Zn_{1-x}Mg_xO$ have a shorter bond to the *c*-axial oxygen atom than to the three lateral oxygen atoms, which is distinct from the coordination of Zn. The precise structure, both local and average, of $Zn_{0.875}Mg_{0.125}O$ obtained from time-of-flight total neutron scattering supports the view that Mg-substitution in ZnO results in increased total spontaneous polarization.

PACS numbers: 71.55.Gs, 77.22.Ej, 78.30.-j, 61.05.fm, 61.05.Qr

I. INTRODUCTION

Research in the area of polar semiconductor heterostructures has been growing rapidly, driven in large part by interest in two-dimensional electron gas (2DEG) systems.[1,2,3,4,5] 2DEGs are known to form at heterojunction interfaces that bear polarization gradients. They can display extremely high electron mobilities, especially at low temperatures, owing to spatial confinement of carrier motions.[6] Recent reports of 2DEG behaviors in $Ga_{1-x}Al_xN$/GaN and $Zn_{1-x}Mg_xO$/ZnO heterostructures have great significance for the development of novel high-electron-mobility transistors (HEMTs)[3,4,5] and quantum Hall devices.[1]

2DEG structures are usually designed by interfacing a polar semiconductor with its less or more polar alloys in an epitaxial manner. Since the quality of the 2DEG depends critically on interface perfection, as well as the polarization gradient at the heterojunction, understanding compositional and structural details of the parent and alloy semiconductors is an important component in 2DEG design and fabrication. The evolution of atomic positions and cell parameters upon alloying can directly affect the magnitude of the polarization gradient and the carrier density at the heterojunction.

$Zn_{1-x}Mg_xO$/ZnO is one of the more promising heterostructure types for studies of 2DEGs, due to the large polarization of ZnO, the relatively small lattice mismatch, and the large conduction band offsets in the $Zn_{1-x}Mg_xO$/ZnO heterointerface. Although 2DEG formation in $Zn_{1-x}Mg_xO$/ZnO heterostructures have been researched for some time, a clear understanding of the alloy structure of $Zn_{1-x}Mg_xO$ is currently lacking. Recently, we have studied composition-dependent changes in the crystal structures of polycrystalline $Zn_{1-x}Mg_xO$ by synchrotron x-ray diffraction and Raman spectroscopy.[7,8] For the composition range $0 \leqslant x \leqslant 0.15$, we have shown that Mg-substitution modifies the aspect ratio of the hexagonal lattice through enhanced bond ionicity, and in parallel, decreases static polarization in the crystal, due to decreased internal distortion in the tetrahedral coordinations.

Here, we conduct a detailed and more precise study of the local structure of $Zn_{1-x}Mg_xO$ alloys using Raman and solid-state nuclear magnetic resonance (NMR), in conjunction with neutron diffraction techniques. Raman and NMR spectroscopy are useful probes for addressing the molecular compositions and structures of solid-solution systems. Peak shapes and widths of the Raman spectra reflect compositional fluctuations and both short- and long-range order, whereas NMR is sensitive to the local environments around specific nuclei. Thus, both techniques can provide structural information on $Zn_{1-x}Mg_xO$ that is complementary to diffraction analyses. Here, we examine the details of E_2^{low} and E_2^{high} Raman modes for $Zn_{1-x}Mg_xO$ (x = 0, 0.05, 0.10, and 0.15). We have also used spin-echo magic-angle-spinning (MAS) ^{67}Zn and ^{25}Mg NMR to study separately zinc and/or magnesium species in ZnO and $Zn_{0.85}Mg_{0.15}O$. These measurements have been correlated with average and local crystal structures of

$Zn_{1-x}Mg_xO$ and ZnO, as established by Rietveld (diffraction space) and pair-distribution-function (PDF, real-space) analyses of time-of-flight neutron diffraction data. Compared with x-rays, neutron scattering provides much greater sensitivity to oxygen and Mg positions, as well as larger momentum transfer as measured by the larger maximum Q wavevector.[9] By taking advantage of the increased data quality, we are able to isolate the geometry of MgO_4 moieties stabilized in the wurtzite ZnO lattice.

II. EXPERIMENTAL

Polycrystalline powder samples of ZnO and $Zn_{1-x}Mg_xO$ (x = 0.05, 0.10, 0.125, and 0.15) were prepared from oxalate precursors obtained by co-precipitation using $Zn(CH_3CO_2)_2{\cdot}2H_2O$, $Mg(NO_3)_2{\cdot}6H_2O$, and $H_2C_2O_4$, all of which had purities of 99.999 % from Aldrich. The two metal salts were dissolved together in deionized water and added to an oxalic acid solution in the ratio of $[Zn^{2+}]$:$[Mg^{2+}]$:$[C_2O_4^{2-}]$ = $(1-x)$:x:1.05. Upon mixing with oxalate, Zn^{2+} and Mg^{2+} immediately coprecipitated as white crystalline oxalate powders, which were washed with deionized water and dried at 60°C for 4 h and subsequently heated at 550°C for 20 h in air to decompose the oxalates to the oxides. Powder x-ray diffraction measurements confirmed the formation of $Zn_{1-x}Mg_xC_2O_4{\cdot}2H_2O$ after heating at 60°C, and $Zn_{1-x}Mg_xO$ after decomposing at 550°C. For the NMR experiments, samples were also prepared at different conditions of temperature (900°C) and atmosphere (O_2, N_2).

Raman spectra for ZnO and $Zn_{1-x}Mg_xO$ (x = 0.05, 0.10, and 0.15) were acquired at room temperature using a Jobin Yvon-Horiba T64000 triple grating (1800 gr/mm) spectrometer. The spectra of lightly compressed powders were recorded using micro-Raman sampling in air with 514.5 nm and 675.5 nm excitations. The spectra reported here were averages of 10 acquisitions of 20 s integrations of the CCD detector with ≈10 mW of laser power focused onto the samples through a 10× objective. There was no evidence of degradation of the samples or associated changes in their spectra under these conditions. The spectrometer was calibrated using a 520.7 cm^{-1} lattice mode of silicon. The Raman features of wurtzite E_2^{low} and E_2^{high} phonon modes were analyzed in detail to determine the peak shape, position, and width. Spectral background was removed following Shirley[10], and the profile fitting was performed using pseudo-Voigt[11] or Breit-Wigner-Fano functions.[12]

NMR measurements of the low-gyromagnetic-ratio nuclei ^{67}Zn and ^{25}Mg were conducted at high (19.6 Tesla) magnetic field strength at the National High Magnetic Field Laboratory in Tallahassee, Florida. These investigations benefited from the enhanced sensitivity and improved resolution for the ^{67}Zn and ^{25}Mg nuclei that results from reduced second-order quadrupolar interactions, which scale inversely with the strength of the high applied magnetic field. The experiments were conducted at room temperature at 19.6 T (^1H resonance frequency of 830 MHz), which for ^{67}Zn ($I = \frac{5}{2}$, 4.1 % natural abundance, *ca.* 1.5 receptivity relative to ^{13}C) and ^{25}Mg ($I = -\frac{5}{2}$, 10.1 % natural abundance, *ca.* 0.7 receptivity relative to ^{13}C) corresponded to Larmor frequencies of 51.88 MHz and 50.76 MHz, respectively. All of the NMR spectra presented here were recorded on a single-resonance 4-mm probehead under MAS conditions at 10 kHz, using a Hahn-echo (*i.e.* $\frac{\pi}{2}$-τ-π-τ-acquisition) with the delays τ set to one rotor period τ_R. The ^{67}Zn and ^{25}Mg shifts were referenced to the bulk external secondary standards ZnSe (274 ppm relative to 1.0 M *aq.* $Zn(NO_3)_2$) and MgO (26 ppm relative to 3.0 M *aq.* $MgSO_4$)[13], respectively. Pulse lengths of 2 μs and 4 μs were used for the $\frac{\pi}{2}$ and π pulses, respectively. A recycle delay of 1 s was used in each case, using 16,000 transients for the ^{67}Zn MAS spectra (*ca.* 5 h each), and 160,000 transients for the ^{25}Mg MAS experiments (*ca.* 46 h each). Second-order quadrupolar MAS lineshapes were fitted using the program DMFIT.[14]

Time-of-flight neutron diffraction data for ZnO and $Zn_{0.875}Mg_{0.125}O$ were obtained on the neutron powder diffractometer NPDF at the Lujan Neutron Scattering Center at Los Alamos National Laboratory. For ease of structural modeling in the PDF analysis of $Zn_{1-x}Mg_xO$, we chose a composition of $x = \frac{1}{8}$ and have used an appropriate 16-atom supercell model of Zn_7MgO_8. For each sample, ≈ 2 g of powder were packed in a vanadium can, and the data were collected for 3 h at 25°C using four detector banks located at 46°, 90°, 119°, and 148°. Control runs, for the intensity corrections, employed an empty vanadium can, a vanadium piece, and air. The program PDFGETN was used to extract the PDF $G(r)$ from the raw scattering data.[15] First, the coherent scattering intensity $I(Q)$ was obtained from raw data by the intensity corrections for container, background, and incident beam. Then, the $I(Q)$ was converted to the structure factor $S(Q)$ by the corrections for sample absorption, multiple scattering, and inelasticity. Finally, the PDF $G(r)$ was constructed by the Fourier transform of the reduced structure factor $F(Q) = Q[S(Q) - 1]$. In the Fourier transform of $F(Q)$ to $G(r)$, Q data were terminated at 35 $Å^{-1}$. PDF refinements were performed using the software program PDFGUI.[16] The average crystal structures of ZnO and $Zn_{0.875}Mg_{0.125}O$ were determined by the Rietveld method using the GSAS-EXPGUI software suite.[17,18]

III. RESULTS AND DISCUSSION

A. Raman spectroscopy

Room temperature Raman spectra for $Zn_{1-x}Mg_xO$ (x = 0, 0.05, 0.10, and 0.15) are shown in Fig. 1, along with mode assignments for the observed peaks.[19,20] The wurtzite lattice, with space group C_{6v}^4 (Hermann-Mauguin symbol $P6_3mc$), has four Raman-active phonon modes, $A_1 + E_1 + 2E_2$. The two E_2 modes are nonpolar, while the A_1 and E_1 modes are polarized along the z-axis and in the xy-plane, respectively.[19,20,21] The polar modes are further split into longitudinal (LO) and transverse (TO) components due to the macroscopic electric field associated with the LO modes. Raman spectra of the ZnO and $Zn_{1-x}Mg_xO$ compounds are dominated by two intense peaks of E_2^{low} (≈ 98 cm^{-1}) and E_2^{high} (≈ 436 cm^{-1}) modes. Raman scattering efficiencies of individual modes in

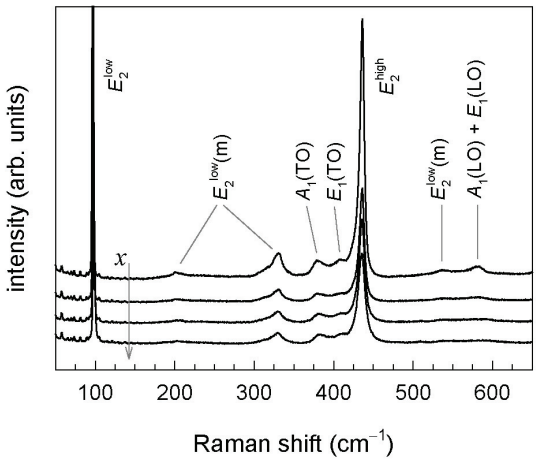

FIG. 1: Raman spectra recorded at room temperature for $Zn_{1-x}Mg_xO$ (x = 0, 0.05, 0.10, and 0.15 from top to bottom). The excitation wavelength used was 514.5 nm.

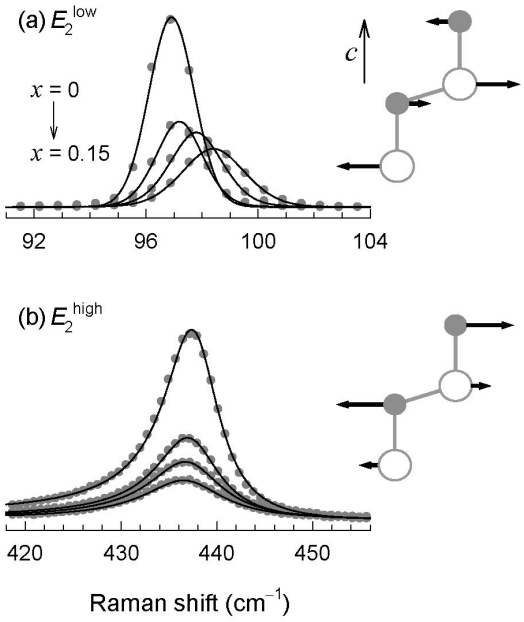

FIG. 2: Line profile fittings for (a) E_2^{low} and (b) E_2^{high} Raman peaks of $Zn_{1-x}Mg_xO$ (observed, gray circles; fit, solid lines; x = 0, 0.05, 0.10, and 0.15 from top to bottom). Simplified lattice vibrations are depicted using large open circles for cations (Zn, Mg) and small gray circles for oxygen.

ZnO are known to vary with the excitation energy.[19] With 514.5 nm (2.41 eV) excitation, the highest Raman efficiencies are observed from E_2^{high} and E_2^{low} modes. However, the polar LO modes exhibit a strong resonance effect as the excitation energy approaches the electronic transition energies. In cases when ultraviolet lasers are used for excitation, the Raman spectra of ZnO or $Zn_{1-x}Mg_xO$ are dominated by the signals from LO modes.[22]

In order to quantify composition-dependent changes in the

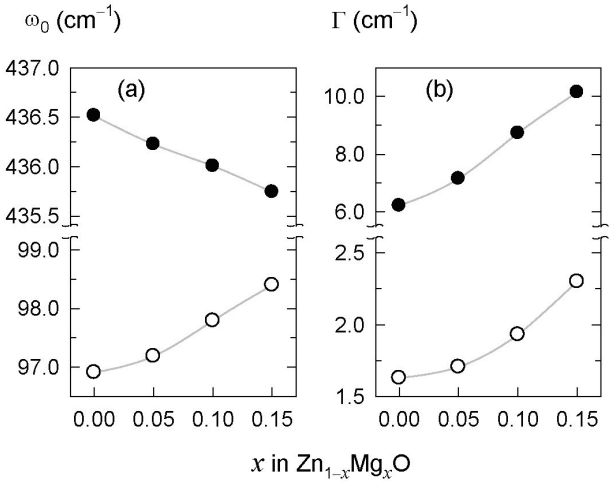

FIG. 3: (a) Raman shifts ω_0 and (b) linewidths Γ for the E_2^{low} (open circles) and E_2^{high} (filled circles) modes of $Zn_{1-x}Mg_xO$.

Raman spectra of $Zn_{1-x}Mg_xO$, the E_2^{low} and E_2^{high} line profiles were analyzed by least-squares fitting with standard peak functions. From the fits, peak position (ω_0) and the full-width-at-half-maximum (FWHM, Γ) linewidths were determined. The profile fittings of both E_2 modes are shown in Fig. 2, and the evolution of peak parameters ω_0 and Γ with Mg-substitution x are plotted in Fig. 3. Consistent with the previous study,[8] the E_2^{high} peaks of $Zn_{1-x}Mg_xO$ are best represented by Lorentzian Breit-Wigner-Fano (BWF) lineshapes with some asymmetry. However, the E_2^{low} line profiles do not fit as well to the Lorentzian-type functions. Instead, the E_2^{low} lines of $Zn_{1-x}Mg_xO$ are found to be pseudo-Voigt-type with predominantly Gaussian components of 97%, 83%, 77%, and 81 % for x = 0, 0.05, 0.10, and 0.15, respectively.

As shown in Fig. 3a, the two E_2 modes of $Zn_{1-x}Mg_xO$ exhibit distinct dependences of phonon energy on the composition. With increased concentration of magnesium, the E_2^{low} mode shows a blueshift, while the E_2^{high} mode exhibits a redshift. For explaining these opposing trends, the vibrational eigenvectors of the wurtzite E_2 modes need to be considered. As shown in Fig. 2, both E_2^{low} and E_2^{high} modes are associated with atomic motions in the *ab*-plane. The lower energy branch corresponds mainly (≈85 %) to the vibrations of heavier components (cations, in case of $Zn_{1-x}Mg_xO$), and conversely the higher energy one corresponds mainly to those of lighter components (oxygen). Consequently, the E_2^{low} mode energy of $Zn_{1-x}Mg_xO$ is explicitly affected by the cationic substitution, according to the reduced mass effect. Replacement of Zn with Mg will decrease the reduced mass of the oscillator and in turn increase the phonon energy. By comparison, the change of cation mass should have less influence on the E_2^{high} mode energy, and its redshift is adequately attributed to the phonon softening caused by the in-plane lattice expansion. As previously reported, the lattice constant a of $Zn_{1-x}Mg_xO$ increases monotonically with x,[7] which appears to account for the observed E_2^{high} mode behavior.

Peak shapes and linewidths of Raman spectra are dictated by the underlying line-broadening mechanisms. Gaussian line broadening is intrinsic to Raman spectra and originates from instrumental resolution. Also, if the sample being examined contains inhomogeneous components with different phonon frequencies, the resulting Raman lineshape would have a Gaussian character, reflecting the statistical nature of the spectrum. On the other hand, Lorentzian line broadening is mostly attributed to finite phonon lifetimes (t), according to the energy-time uncertainty relationship $\Gamma/\hbar = 1/t$. The phonon lifetime shortening, which will cause linewidth broadening, can occur *via* two independent phonon decay mechanisms; by anharmonic decay into other Brillouin zone phonons or by phonon disruption at crystal defects. The latter, involving lattice imperfections, are quite common for alloy and solid-solution systems. Specifically for $Zn_{1-x}Mg_xO$, it is expected that Mg-substitution will substantially reduce the size of ordered domains, and thereby block the long-range propagation of zone center phonons.

As noted above, the E_2^{low} and E_2^{high} lines of ZnO are respectively fitted with Gaussian and Lorentzian functions. It indicates that the E_2^{high} mode of ZnO has anharmonic phonon decay channels, whereas the E_2^{low} phonon does not. The Lorentzian line broadening behavior of E_2^{high} mode, in Fig. 3b, further manifests that the Mg-substitution increasingly populates the phonon field of $Zn_{1-x}Mg_xO$ with defect centers. The E_2^{low} mode also undergoes a gradual line broadening with x, and its peak shape changes upon Mg-substitution. While unsubstituted ZnO displays a nearly pure Gaussian peak for the E_2^{low} mode, the peaks from $Zn_{1-x}Mg_xO$ ($x > 0$) samples are found to contain ≈20 % of Lorentzian components. Therefore we conclude that, for the $Zn_{1-x}Mg_xO$ system, the same line broadening mechanism applies to both E_2^{low} and E_2^{high} modes: phonon lifetime shortening by increased crystal defects upon Mg substitution.

B. Solid-state ^{67}Zn and ^{25}Mg NMR spectroscopy

A different view of the disorder induced by Mg-substitution in ZnO materials can be obtained from solid-state NMR, using the NMR-active isotopes ^{25}Mg (spin $I = -\frac{5}{2}$) and ^{67}Zn ($I = \frac{5}{2}$). These nuclei are challenging to observe, because their low natural abundances and low gyromagnetic ratios (see Experimental) yield low signal sensitivities, and because second-order quadrupolar interactions associated with nuclear spins $|I| > \frac{1}{2}$ can lead to a dramatic broadening of their NMR spectra. Second-order quadrupolar effects, however, scale with the inverse of the static magnetic field B_0, and are therefore mitigated at high magnetic fields, which also increase signal sensitivity.

Solid-state ^{67}Zn MAS NMR spectra acquired at 19.6 T of ZnO and $Zn_{0.85}Mg_{0.15}O$ are shown in Fig. 4. The materials were prepared by heating at 900°C in N_2 and yield similar spectra that clearly exhibit scaled second-order quadrupolar powder MAS lineshape features.[23] Associated values for the isotropic ^{67}Zn chemical shift, δ_{iso}, the quadrupolar coupling

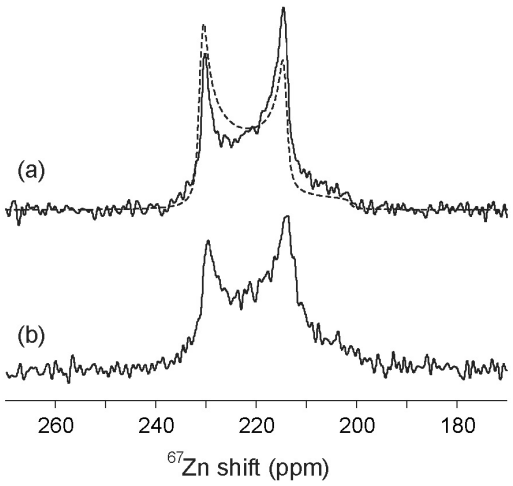

FIG. 4: Solid-state spin-echo ^{67}Zn MAS NMR spectra acquired at 19.6 T, room temperature, and 10 kHz MAS: (a) ZnO and (b) $Zn_{0.85}Mg_{0.15}O$ powders, both prepared at 900°C in N_2. Accompanying the ZnO spectrum in (a) is a fit (dashed line) of the experimental lineshape to a simulated second-order quadrupolar powder pattern.

constant, ν_Q, and the asymmetry parameter, η_Q, can be determined by fitting each resolved second-order quadrupolar MAS lineshape. A simulated powder pattern is shown as the dashed line in Fig. 4a accompanying the ^{67}Zn MAS spectrum of ZnO and corresponding to the calculated values δ_{iso} = 236 ppm, ν_Q = 378 kHz, and η_Q = 0.1. Several discrepancies between the calculated and experimental powder patterns may be due to modest anisotropy of the powder particles and/or to uneven excitation of the different crystallite orientations by the radiofrequency pulses. The powder pattern and fit parameters are nevertheless consistent with a single crystallographically distinct and relatively symmetric ^{67}Zn site in the wurtzite ZnO structure. The ^{67}Zn MAS spectrum of $Zn_{0.85}Mg_{0.15}O$ in Fig. 4b exhibits a similar lineshape and features, which are broadened by the presumably random incorporation of Mg atoms within the Zn-rich wurtzite lattice.

The close similarity between the ^{67}Zn MAS NMR spectra of ZnO (Fig. 4a) and $Zn_{0.85}Mg_{0.15}O$ (Fig. 4b) indicates that the substitution of 15 % of Zn atoms by Mg has little influence on the local electronic environments of a majority of the ^{67}Zn nuclei. Assuming that Mg atoms are distributed randomly, the probability of having no Mg atom in the second coordination sphere of a given ^{67}Zn nucleus is only 14 % (the first coordination sphere consisting of four O atoms). Significant effects on the ^{67}Zn spectrum would be expected if the quadrupolar interactions were substantially perturbed by the substitution of Mg atoms for 1, 2, 3, 4 (probabilities of 30 %, 29 %, 17 %, and 7 %, respectively) or more of the 12 Zn atoms in the second coordination sphere. However, despite the high probability of modifications of the local chemical environment of the ^{67}Zn nuclei upon 15 % Mg-substitution, dramatic changes of the ^{67}Zn spectrum are not observed, rather only modest broadening that reflects increased disorder. Under these conditions, the differences induced in ZnO or $Zn_{0.85}Mg_{0.15}O$ by changing the synthesis atmosphere (*e.g.*, air, O_2, or N_2) and temperature

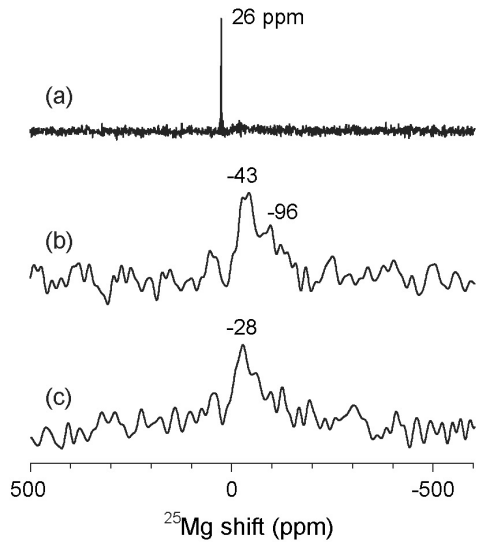

FIG. 5: Spin-echo ^{25}Mg MAS NMR spectra, recorded at 19.6 T, of (a) polycrystalline MgO powder (external reference for ^{25}Mg NMR shift), (b) $Zn_{0.85}Mg_{0.15}O$ powder prepared at 550°C in air, and (c) $Zn_{0.85}Mg_{0.15}O$ powder prepared at 900°C in N_2.

(over the range 550°C to 900°C) were too subtle to be clearly reflected in the corresponding ^{67}Zn MAS NMR spectra (data not shown), which are similar to those in Fig. 4a, b. Thus, it appears that ^{67}Zn NMR measurements of these ZnO-related materials are sensitive principally to substitutions that result in modifications of the first coordination sphere of the zinc nuclei (substitution of the anionic species), or to substitutions resulting in larger lattice distortions or increased electronic disorder than observed here.[24]

Solid-state ^{25}Mg MAS NMR measurements complement the ^{67}Zn NMR results by being sensitive to the structural and electronic perturbations experienced directly by Mg atom incorporated into ZnO lattices. The ^{25}Mg MAS NMR measurements were similarly conducted at 19.6 T and the resulting spectra are shown in Fig. 5 for polycrystalline MgO and different $Zn_{0.85}Mg_{0.15}O$ powders prepared at 550°C in air and at 900°C in N_2. The ^{25}Mg MAS spectrum in Fig. 5a of MgO shows a narrow well-defined ^{25}Mg peak that reflects the highly symmetric coordination environment of the single type of Mg site in its rock-salt structure.[25] By comparison, the ^{25}Mg MAS spectra of the different $Zn_{0.85}Mg_{0.15}O$ powders contain broad and relatively unstructured lineshapes centered at *ca.* −30 ppm to −40 ppm that reflect broad distributions of signal intensity and thus broad distributions of local ^{25}Mg environments. The first Mg coordination sphere (MgO_4) in $Zn_{0.85}Mg_{0.15}O$ is expected to be significantly distorted from its regular tetrahedral geometry, and the second coordination sphere, composed of $Mg(Zn,Mg)_{12}$, is expected to have an even larger number of different local configurations, bond distances, and/or bond angles. The ^{25}Mg MAS NMR spectra appear to be more sensitive than the ^{67}Zn NMR results to local material environments in $Zn_{0.85}Mg_{0.15}O$. However, the low signal-to-noise and broad lines observed for natural abundance ^{25}Mg in $Zn_{0.85}Mg_{0.15}O$, even at 19.6 T, preclude a detailed and reliable analysis of the isotropic shift distributions and second-order quadrupolar broadening that would be necessary to extract directly quantitative information on nature of the Mg site distributions and/or their disorder. It is noteworthy that the $Zn_{0.85}Mg_{0.15}O$ powders do not display any spectral feature corresponding to bulk MgO, thereby ensuring the phase purity of $Zn_{1-x}Mg_xO$ ($x \leqslant 0.15$) solid solutions, within the sensitivity limit of the ^{25}Mg NMR measurements.[26]

In common for ^{29}Si, ^{27}Al, and ^{25}Mg, an increase of the coordination number for a given cationic center counts for enhanced local shielding, resulting in an upfield displacement of the signal(s) to lower shift values.[13,27] The spinel $MgAl_2O_4$ containing MgO_4 fragments exhibits a ^{25}Mg shift of 52 ppm, compared to 26 ppm for MgO which is comprised of MgO_6 local units.[13] By comparison, clay minerals in which Mg atoms are coordinated by six (O,OH) ligands yield ^{25}Mg shifts in the range of 0 to −100 ppm.[25] The wurtzite oxide $Zn_{0.85}Mg_{0.15}O$ has a 4-coordinated geometry of Mg, similar to $MgAl_2O_4$, but the former clearly shows a more upfield-shifted ^{25}Mg resonance at $-30 \sim -40$ ppm. We infer that ^{25}Mg MAS NMR signals are considerably influenced by the ligand identity beyond the first coordination shell, and that Zn has a far stronger shielding contribution than Al, Si, or alkaline-earths, thus accounting for the observed resonance values.

C. Neutron diffraction

In previous studies, the crystal structure of ZnO has been reported [space group $P6_3mc$, Zn at $(\frac{1}{3}\frac{2}{3}0)$ and O at $(\frac{1}{3}\frac{2}{3}u)$] with lattice constants of $a = 3.2427\sim3.2501$ Å and $c = 5.1948\sim5.2071$ Å, and atomic position parameter $u = 0.381\sim0.3826$.[28,29,30,31,32,33] In our previous synchrotron x-ray study on polycrystalline ZnO, we obtained $a = 3.2503$ Å, $c = 5.2072$ Å, and $u = 0.3829$.[7] Here, we reexamine the crystal structures of polycrystalline ZnO and $Zn_{0.875}Mg_{0.125}O$ utilizing neutron scattering, which has several advantages over x-rays. The coherent neutron scattering length of O (5.804 fm) is comparable to those of Zn (5.680 fm) and Mg (5.375 fm),[34] as distinct from x-ray diffraction, where scattering is strongly weighted by Zn. Moreover, neutron scattering can provide high Q diffraction data with much less attenuation than x-rays, due to there being no fall-off with Q in the form factor.

Rietveld refinements of ZnO and $Zn_{0.875}Mg_{0.125}O$ were carried out on four histograms of data collected at detector locations of 46°, 90°, 119°, and 148°. The highest-Q data from the 148° detector covers the range of $d > 0.25$ Å ($Q < 25$ Å^{-1}). The model used for the refinement in space group $P6_3mc$ has Zn/Mg at the 2*b* Wyckoff position $(\frac{1}{3}\frac{2}{3}0)$ and O also at 2*b* position $(\frac{1}{3}\frac{2}{3}u)$. For $Zn_{0.875}Mg_{0.125}O$, Zn and Mg were statistically distributed over the common site with fractional occupancies fixed to the respective compositions. The refinement converged with reliability factors of $R_{wp} = 2.57\,\%, R_p = 1.80\,\%$, and $\chi^2 = 2.71$ for ZnO, and $R_{wp} = 2.89\,\%, R_p = 2.04\,\%$, and $\chi^2 = 3.56$ for $Zn_{0.875}Mg_{0.125}O$. The Rietveld refinement profiles and the structural parameters are given in Fig. 6 and Table I, respectively. The present refinement results agree

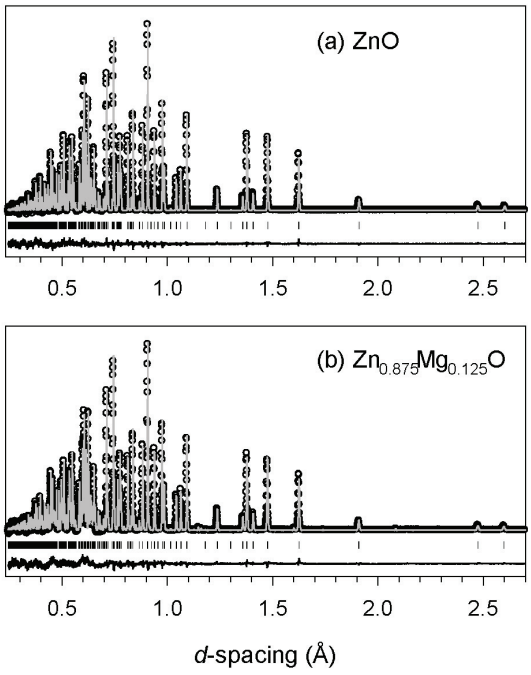

FIG. 6: Rietveld refinement of time-of-flight powder neutron diffraction profiles of (a) ZnO and (b) $Zn_{0.875}Mg_{0.125}O$. Calculated patterns (gray lines) are superimposed on observed data (open circles), with Bragg positions and difference profiles at the bottom.

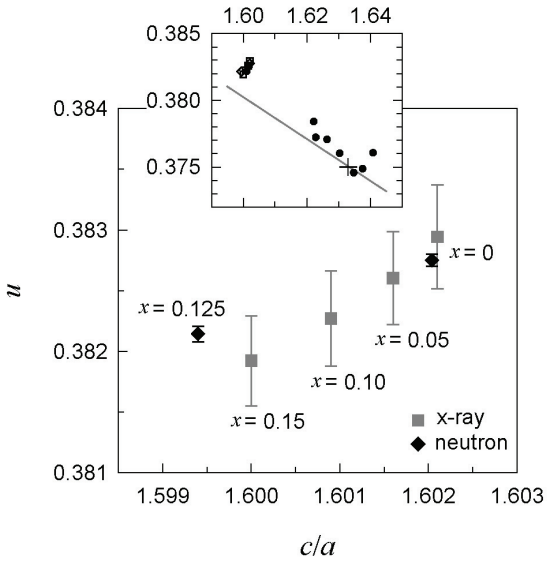

FIG. 7: Average wurtzite parameters c/a and u of ZnO and $Zn_{1-x}Mg_xO$ determined by Rietveld refinements of neutron (diamonds) and synchrotron x-ray (squares, ref. [7]) diffraction patterns. Note the significantly smaller error bars that emerge from the neutron study. The inset shows the data observed from existing wurtzites (see ref. [7] for details).

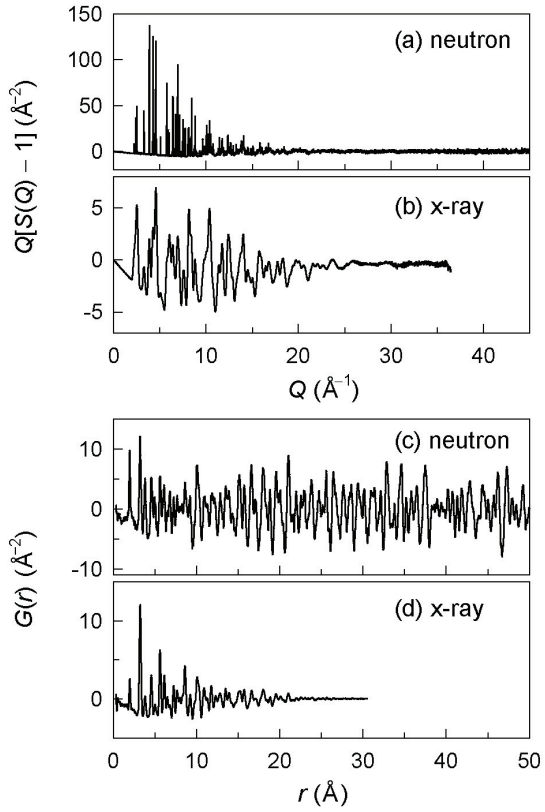

FIG. 8: Comparison of high-Q scattering data from ZnO measured using synchrotron x-ray and pulsed-neutron radiation: (a,b) $F(Q) = Q[S(Q)-1]$, and (c,d) $G(r)$. In the Fourier transform of $F(Q)$ to $G(r)$, Q data were terminated at 28 Å^{-1} for x-rays, and 35 Å^{-1} for neutrons.

well with the findings from our previous synchrotron x-ray study.[7] Both studies indicate that Mg-substitution expands the a-parameter, compresses the c-parameter, and decreases the oxygen position parameter u, as summed up in Fig. 7. The two data sets from x-ray and neutron reveal an identical trend in the structural evolution in terms of a, c, and u.

TABLE I: Structural parameters for ZnO and $Zn_{0.875}Mg_{0.125}O$ determined from the Rietveld refinement of time-of-flight neutron diffraction pattern.

	ZnO	$Zn_{0.875}Mg_{0.125}O$
V (Å^3)	47.603(1)	47.578(1)
a (Å)	3.24945(1)	3.25058(2)
c (Å)	5.20574(3)	5.19771(3)
c/a	1.60204	1.59940
u	0.38275(5)	0.38214(6)
U_{iso}(Zn/Mg) (Å^2)	0.00648(8)	0.0065(2)
U_{iso}(O) (Å^2)	0.0101(1)	0.0087(2)
d_{M-O} (Å)	(1×) 1.9925(3)	(1×) 1.9868(3)
	(3×) 1.9729(1)	(3×) 1.9743(1)
$\angle_{O-M-O}$ (°)	108.022(7)	108.081(9)
	110.881(7)	110.825(9)

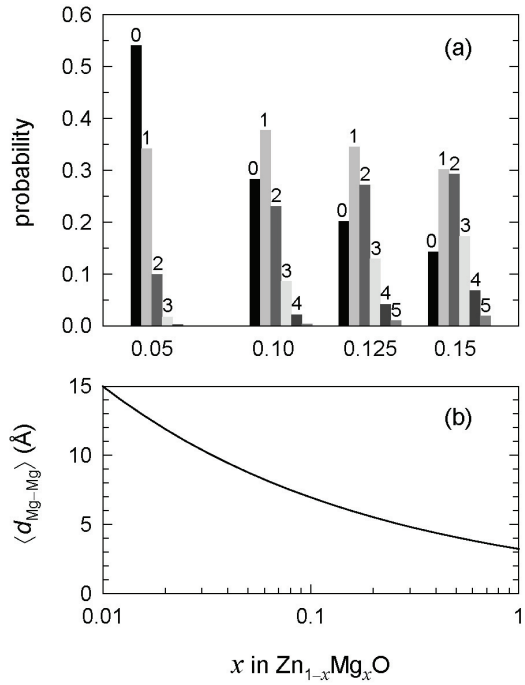

FIG. 9: (a) Probability for a cation in $Zn_{1-x}Mg_xO$ to have 0, 1, 2, 3, 4 or 5 Mg neighbors in the 12-membered coordination shell ($r \approx 3.25$ Å), and (b) mean separation between the nearest Mg−Mg pairs.

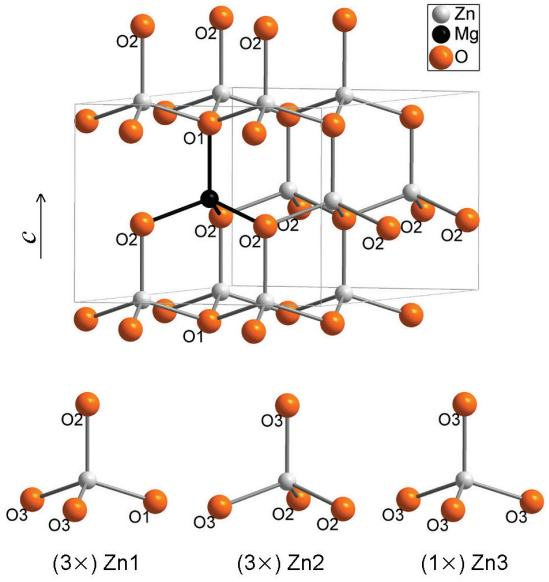

FIG. 10: (Color online) Zn_7MgO_8 supercell model structure used for neutron PDF analyses of $Zn_{0.875}Mg_{0.125}O$, and coordination environments for three distinct Zn sites therein. In the top part, unlabeled oxygen atoms belong to the O3 type (see text).

For the composition range up to $x = 0.15$, the $Zn_{1-x}Mg_xO$ solid solutions remain isostructural with wurtzite ZnO, with both Zn and Mg tetrahedrally coordinated by O atoms. However, since the two cations Zn and Mg have clearly distinct crystal chemistries in oxidic environments, it is conjectured that they may have distinct local geometries within $Zn_{1-x}Mg_xO$ lattices. In order to directly address this question, we have carried out neutron PDF analyses of $Zn_{0.875}Mg_{0.125}O$ and ZnO. Figure 8 shows the PDF data for ZnO, comparing the present neutron data with the x-ray data previously measured at Beamline 11-ID-B of the Advanced Photon Source at Argonne National Laboratory. As can be seen from Figs. 8a and 8b, the neutron study provides scattering information over a significantly higher Q range and also with higher resolution. Correspondingly, the neutron PDF $G(r)$ can be obtained for far wider r-ranges than when using x-rays (Fig. 8c). Given this, neutrons are expected to enable better description of the $Zn_{1-x}Mg_xO$ alloy structure(s).

In order to obtain an appropriate real-space model for the PDF analysis of $Zn_{0.875}Mg_{0.125}O$, we estimate as follows, the impact of Mg-substitution on the chemical environment within the ZnO lattice. Cations in the wurtzite lattice form a hexagonal close-packed sublattice, where each cation has 12 nearest neighbors. At the Mg-substitution level of $x = 0.125$, it is estimated that ≈80 % of the cations have at least one Mg neighbor in the cation sublattice (Fig. 9). Each cation (whether Zn or Mg) has as neighbors, 1.5 Mg atoms on average, and the mean Mg−Mg distance is as short as 6.5 Å. Therefore the coordination geometry of MgO_4 will serve a substantial structural factor in the PDF of $Zn_{0.875}Mg_{0.125}O$ and needs to be treated with independent parameters in the PDF refinement.

On the basis of the above considerations, the structural model for $Zn_{0.875}Mg_{0.125}O$ was designed as follows. To distinguish the Mg and Zn atoms in the unit cell, while maintaining the composition, a $2\times2\times1$ supercell of the primitive wurtzite structure was selected, with the cell parameters $a = b \approx 6.5$ Å, $c \approx 5.205$ Å, $\alpha = \beta = 90°$, $\gamma = 120°$, and the unit content Zn_7MgO_8. In the average structure scheme, in which the atomic positions are set as $(\frac{1}{3}\,\frac{2}{3}0)$ for cations and $(\frac{1}{3}\,\frac{2}{3}u)$ for anions, the external and internal geometries of all the tetrahedra are uniformly defined by the c/a ratio and u, respectively. However in the supercell model, we allowed the MgO_4 unit to have its own coordination geometry, irrespective of the ZnO_4 geometry. As a result, the eight O atoms in the supercell unit are divided into three groups; one O atom bonded to Mg along the c-axis (O1), three O atoms bonded to Mg laterally (O2), and the remaining four O atoms (O3). The seven Zn atoms are also grouped according to their proximities to the Mg atom; three Zn atoms having an apical O2 oxygen atom (Zn1), three Zn atoms bonded to O2 atoms laterally (Zn2), and one Zn bonded to only O3 atoms (Zn3). Figure 10 illustrates the supercell configuration and the three different types of ZnO_4 geometries.

The PDF of ZnO was analyzed using a simple wurtzite cell (Zn_2O_2) obeying the symmetry requirements of the $P6_3mc$ space group. However, for the supercell refinement of $Zn_{0.875}Mg_{0.125}O$, several symmetry constraints were lifted from the average structure description. The z-coordinates of the O1, O2, and O3 types of oxygen atoms were independently varied, and the z-coordinate of Mg was also refined. We also attempted in-plane displacements of the O2 atoms,

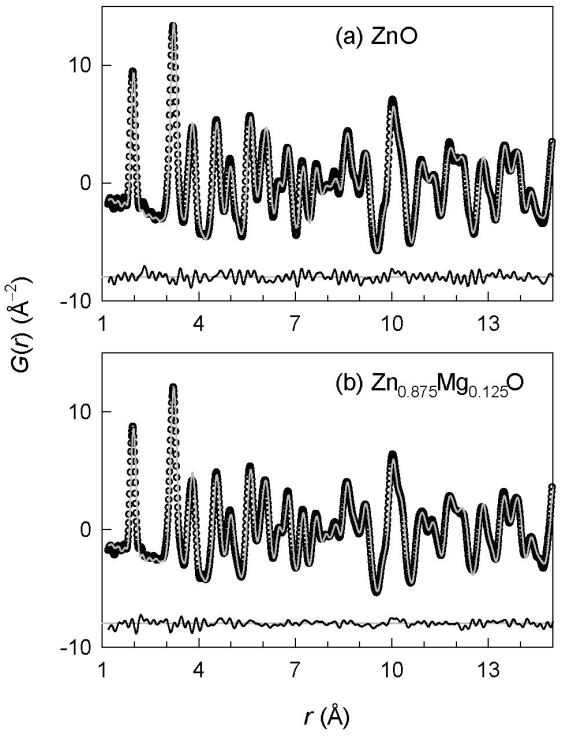

FIG. 11: Neutron PDF refinements for (a) ZnO and (b) $Zn_{0.875}Mg_{0.125}O$, parts of the 1.2−22 Å fittings. Calculated PDFs (gray lines) are superimposed on experimental data (open circles), with the differences shown at the bottom of each.

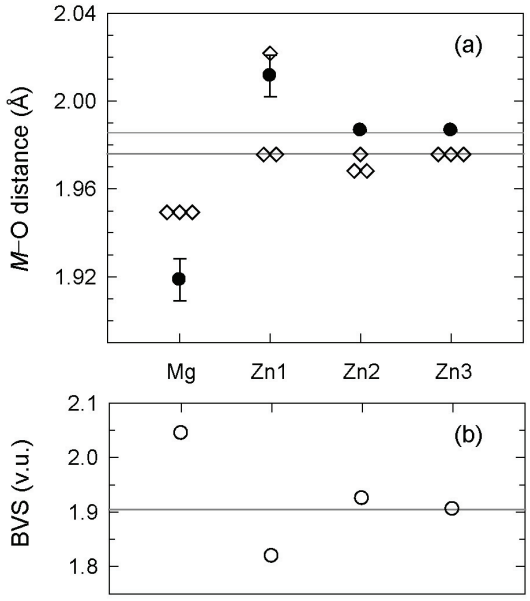

FIG. 12: (a) Mg−O and Zn−O bond distances in $Zn_{0.875}Mg_{0.125}O$, as analyzed by the neutron PDF refinement of a Zn_7MgO_8 supercell model (c-axial bonds, circles; lateral bonds, diamonds), and (b) bond valence sums for each cation site. Horizontal lines indicate the Zn−O bond distances (in the upper panel) and BVS for Zn (in the lower panel) in ZnO.

but found that these were unstable in the refinement. Therefore, the refinement for $Zn_{0.875}Mg_{0.125}O$ included three more position parameters than those for ZnO. For both ZnO and $Zn_{0.875}Mg_{0.125}O$, the refinements of $G(r)$ used the variables of lattice constants, atomic position parameters, isotropic temperature factors, structure scale factor, and peak sharpening coefficients.

Figure 11 shows the neutron PDF refinements for ZnO and $Zn_{0.875}Mg_{0.125}O$, carried out in the r range of 1.2 Å to 22 Å. The refinement parameters are summarized in Table II. For both structures, the refinements were achieved with satisfactorily low R_w's of 7.9 % (ZnO) and 8.3 % ($Zn_{0.875}Mg_{0.125}O$). In comparison with the Rietveld results, the PDF-refined lattice constants are systematically larger by ≈0.06 %, but good agreements are observed for the c/a ratios. Also, the oxygen atom position in ZnO is reasonably well reproduced from the PDF and Rietveld refinements. An interesting finding emerges from the atomic coordinates of Mg and its adjacent oxygen atoms (O1 and O2) in $Zn_{0.875}Mg_{0.125}O$. As found in Table II, the three groups of O atoms have clearly distinct z-coordinates from one another. Both the O1 and O2 groups are vertically shifted towards their respective Mg atoms. Mg itself also moves towards the basal plane formed of O2 atoms. The resulting MgO_4 unit has a squashed tetrahedral geometry (point group C_{3v}), with a much shorter height than those of ZnO_4 tetrahedra. However the O3 atoms, which are not directly bonded to Mg, have similar z-coordinates to those found in ZnO. Therefore, the $(Zn3)(O3)_4$ tetrahedra retain the unperturbed geometry of ZnO. The other types of ZnO_4 tetrahedra share corners with MgO_4 and are likely to undergo intermediate distortion.

To examine the presence of short-range structural characteristics, the PDF refinements were carried out from 1.2 Å to different values of r_{max} between 10−30 Å. The lattice constants and position parameters showed insignificant variations with r_{max}, and the R_w values had shallow minima at $r_{max} \approx 22$ Å for both ZnO and $Zn_{0.875}Mg_{0.125}O$. The Mg−O and Zn−O bond distances plotted in Fig. 12 represent the averaged results of multiple refinements over 1.2−r_{max} (Å), where r_{max} was increased from 10 to 30 Å in 2 Å steps. From Fig. 12a, we

TABLE II: Structural parameters from the neutron PDF refinements of ZnO and $Zn_{0.875}Mg_{0.125}O$, over the r range of 1.2−22 Å.

	ZnO	$Zn_{0.875}Mg_{0.125}O$
a (Å)	3.2514(3)	3.2527(4) × 2
c (Å)	5.2089(6)	5.2015(8)
c/a	1.6020	1.5991
z(O)	0.3824(4)/0.8824(4)	0.3825(8)/0.8825(8) (O3)
		0.386(3) (O2)
		0.858(5) (O1)
z(Mg)		0.486(8)
U_{iso}(Zn/Mg) (Å^2)	0.0086(8)	0.0063(6)
U_{iso}(O) (Å^2)	0.0070(6)	0.0081(8)

find a meaningful distinction between the MgO_4 and ZnO_4 bonding structures. The Mg−O bonds are shorter than the Zn−O bonds, and the former set consists of one short and three longer bonds, in contrast to the latter. These results are consistent with the greater sensitivity of the ^{25}Mg NMR spectra (Fig. 5b, c) to Mg substitution into ZnO-rich lattices, compared to the ^{67}Zn NMR results (Fig. 4). For Mg and the three Zn atom types in $Zn_{0.875}Mg_{0.125}O$, bond valence sums (BVS)[35] are evaluated, as shown in Fig. 12b. The valence sums for all of the cation and anion sites in $Zn_{0.875}Mg_{0.125}O$ are within a reasonable range around the ideal magnitude of 2 valence units (v.u.). The relatively underbonded situation for Zn1 atoms and the slight overbonding of the Mg atom are the results of a rather drastic shift of the bridging O1 atom. The global instability index (GII)[35] of $Zn_{0.875}Mg_{0.125}O$ is calculated as 0.116 v.u., which is significantly larger than that of ZnO (0.067 v.u.). The GII value is often used as a measure of the residual bond strain, and is known not to exceed 0.2 v.u. for ordinary structures in the standard state.[35,36] It is worth mentioning, in light of the above GII considerations, that the increased microstrain upon Mg-substitution results in characteristic optical and x-ray line broadening behavior of $Zn_{1-x}Mg_xO$ that we have previously reported.[37,38]

The solid solution of $Zn_{1-x}Mg_xO$ has the thermodynamic solubility limit of $x \approx 15$ % on the ZnO-rich side. Obviously the distinct coordination preferences of Mg and Zn prevent the formation of a continuous solid solution across the entire composition range, x. While Mg has a point symmetry of O_h in its binary oxide MgO, wurtzite ZnO possesses only a C_{3v} environment. Here, we rationalize the neutron PDF result for the MgO_4 tetrahedral geometry, in several ways. Both bond valence[39] and ionic radii[40] compilations are useful to explain the smaller tetrahedral volume of MgO_4, as compared with ZnO_4. The bond valence parameter of Mg−O (R_0 = 0.693 Å) is smaller than that of Zn−O (R_0 = 0.704 Å), implying that in general Mg−O bonds are shorter than Zn−O bonds, for the same coordination numbers. Similarly, the 4-coordinate ionic radius of Mg^{2+} (0.57 Å) is smaller than that of Zn^{2+} (0.60 Å). In order for the MgO_4 tetrahedron to have a smaller volume than ZnO_4, either the tetrahedral height or the base area should shrink, or an isotropic volume change could occur. From the PDF analysis, the c parameter around Mg showed a clear decrease, whereas the a parameter appears to be nearly unchanged. The c-axial parameter contraction of MgO_4 unit can be deduced also from the composition-dependent changes of the average structure of $Zn_{1-x}Mg_xO$.

The variable u is the only position parameter in the wurtzite structure. It corresponds to the ratio of the apical bond distance to the c length, d_{apical}/c, or $d_{\mathrm{apical}}/2h$, where h is the height of the tetrahedron. For $Zn_{0.875}Mg_{0.125}O$, u(Mg) is determined to be 0.395, a value that finds no correspondence to the experimental structures of pure wurtzites. Existing wurtzites have u values within the range of 0.374 to 0.383. Such a high u found for MgO_4 is closely linked with its extremely small aspect ratio ($2h/a$ = 1.509, as compared to the ideal value 1.633). To compare the potential fields within the tetrahedral spaces of MgO_4 and ZnO_4, the valence sums of Mg and Zn were calculated as functions of u (Fig. 13). In

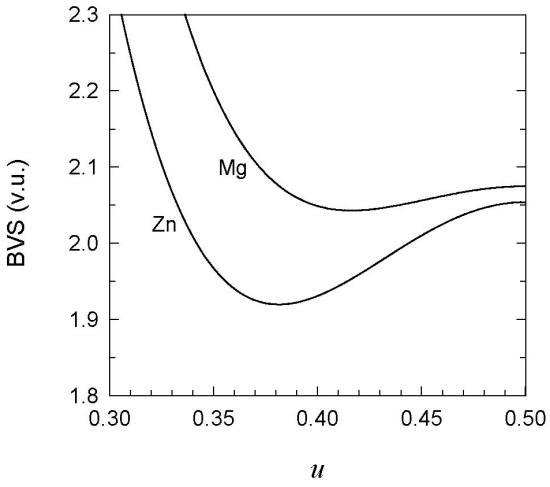

FIG. 13: u-dependent bond valence sums for Mg and Zn in the tetrahedral spaces of their oxides. The dimensions of MgO_4 and ZnO_4 tetrahedra are from the neutron PDF refinements of $Zn_{0.875}Mg_{0.125}O$ and ZnO, respectively. For u near 0.5, a fifth oxygen atom was added to the coordination shell to account for the pseudo-bipyramidal configuration.

ZnO, the tetrahedral cavity is slightly oversized for Zn, and the BVS(Zn) has a minimum of ≈1.9 v.u. at $u \approx 0.382$. The potential minimum suggested by BVS(Zn) is in a good agreement with the experimental u for ZnO. However, the MgO_4 shell in $Zn_{1-x}Mg_xO$ is rather small for Mg, resulting in a global overbonding situation. The BVS(Mg) is minimized at a markedly higher u range than for BVS(Zn), making it clear why the experimental u(Mg) is conspicuously larger than u(Zn).

Several authors have used first-principles density functional theory (DFT) to predict the relaxed structure of hypothetical wurtzite MgO.[41,42,43] An earlier DFT study attempted to relax the energy-minimized wurtzite MgO structure, but only to obtain a hexagonal structure corresponding to the limit of c-axis compression (c/a = 1.20, u = 0.5).[41] However in later studies, the energy minimizations for wurtzite MgO were achieved within appropriate boundary conditions; c/a = 1.514, u = 0.398 by Janotti *et al.*[42], and c/a = 1.520, u = 0.395 by Gopal and Spaldin[43]. Therefore, wurtzite MgO, if it ever occurs, is expected to have an abnormally small c/a ratio and large u value, compared with common wurtzites including ZnO. Interestingly, the above computational approximations of the hexagonal MgO structure agree well with our PDF analyses of $Zn_{1-x}Mg_xO$, which underscores that the MgO_4 fragment has smaller c/a and larger u than ZnO_4. Malashevich and Vanderbilt[44] and Fan *et al.*[45] performed DFT computations of $Zn_{1-x}Mg_xO$ supercell models, also deriving consistent conclusions that c/a decreases with Mg-substitution, and that u(Mg) > u(Zn). The results from the neutron PDF refinement and the above DFT computations are plotted together in Fig. 14, in which the distinct internal/external geometries of MgO_4 and ZnO_4 are contrasted. As a general trend, isolated MgO_4 tetrahedra always have larger u parameters than ZnO_4 units. The extremely good agreement between the *local* coor-

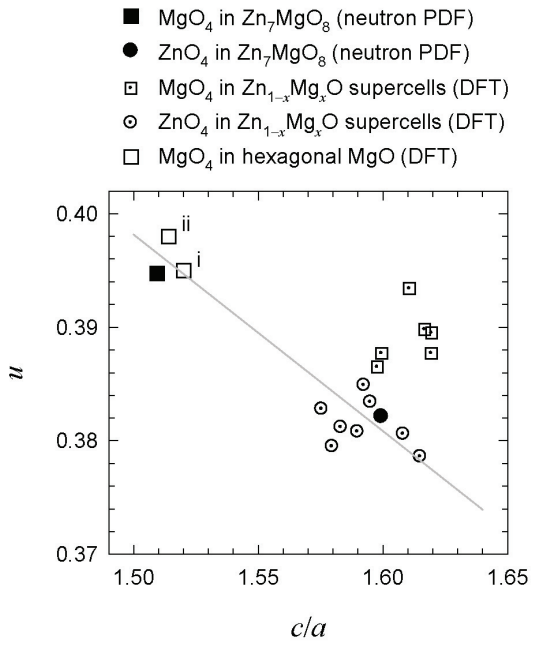

FIG. 14: Aspect ratio c/a and internal parameter u for MgO_4 (filled squares) and ZnO_4 (filled circles) tetrahedra in $Zn_{0.875}Mg_{0.125}O$, as analyzed by neutron PDF refinements. DFT results for wurtzite MgO and $Zn_{1-x}Mg_xO$ supercells are compared together: Open squares correspond to the MgO_4 geometry in hexagonal MgO (i: ref.[42] and ii: ref.[43]), and the dotted open squares and dotted open circles represent the MgO_4 and ZnO_4 geometries found in $Zn_{1-x}Mg_xO$ supercells[46], respectively. The gray line defines the border where the axial cation-anion bond along c and three equatorial bonds become equidistant.

dination of Mg in $Zn_{0.875}Mg_{0.125}O$ determined here from PDF studies and DFT calculations on end-member wurtzite MgO is remarkable. This is in part attributed to our use of the ratio c/a as a comparison parameter. This ratio has fewer systematic errors than do the values of the lattice parameters taken separately.

The total polarization P_s of polar oxides can be broken down into electronic, ionic, and piezoelectric contributions, related respectively to the polarizability of component ions, ionic arrangements, and lattice parameters. Mg-substitution decreases the electronic polarization (P_{el}) of ZnO, because of its greater ionic character, whereas the concomitant c-axis compression is expected to increase the piezoelectric polarization (P_{pz}). Quantitative estimation of the above two contributions (P_{el}, P_{pz}) requires sophisticated theoretical analyses and cannot be provided here for ZnO and $Zn_{0.875}Mg_{0.125}O$. Meanwhile, the ionic polarization (P_{ion}) of $Zn_{1-x}Mg_xO$ can be approximated by a simple electrostatic model using the c-axial positions of Zn, Mg, and O. We calculated P_s of $Zn_{0.875}Mg_{0.125}O$ and ZnO, assuming point charges ($q = +2$ for Zn and Mg, and -2 for O), and using the atomic coordinates as determined by neutron PDF analysis (see Appendix). Separate reference structures were used for ZnO and $Zn_{0.875}Mg_{0.125}O$, with the corresponding experimental a and c values, but with $u = 0.375$, so that within isolated $(Zn,Mg)O_4$ moieties the net centers of the cation and anion charges coincide. The calculated P_s values ($= P_{ion}$ here), along c, are $-5.18\,\mu C/cm^2$ for ZnO and $-5.25\,\mu C/cm^2$ for $Zn_{0.875}Mg_{0.125}O$ ($\Delta P_{ion} = -0.07\,\mu C/cm^2$). For comparison, Malashevich and Vanderbilt[44] have employed the Berry-phase approach, to obtain electric polarization of a Zn_5MgO_6 ($x = \frac{1}{6}$) supercell. They find $\Delta P_{ion} = -0.22\,\mu C/cm^2$, $\Delta P_{el} = +0.01\,\mu C/cm^2$, and $\Delta P_{pz} = -0.81\,\mu C/cm^2$, relative to $P_s(ZnO) = -3.22\,\mu C/cm^2$. In fact, the following relations hold true in general for other $Zn_{1-x}Mg_xO$ supercells ($x = \frac{1}{4}, \frac{1}{3}, \frac{1}{2}$) studied by them: $\Delta P_{el} > 0$, $\Delta P_{ion} < 0$, $\Delta P_{pz} < 0$, and $|\Delta P_{el}| \ll |\Delta P_{ion}| < |\Delta P_{pz}|$. We therefore expect that the total polarization of $Zn_{1-x}Mg_xO$ should be larger than that of ZnO, with the increases of piezoelectric and ionic polarizations dominating the decrease of the electronic contribution. We note that P_s(ZnO) from Malashevich and Vanderbilt differs somewhat from the results of other DFT studies[43,47,48,49] which reported $P_s(ZnO) = -5.0 \sim -5.7\,\mu C/cm^2$. But since we are primarily interested in the relative portions of P_{el}, P_{ion}, and P_{pz} in the P_s, and their changes with respect to the Mg-substitution in ZnO, we ignore the small discrepancies in the absolute values.

The result, an increase of P_{ion} upon Mg-substitution, differs from our previous estimates based solely on synchrotron x-ray diffraction analyses.[7,8] This inconsistency arises mostly from the improved models for the $Zn_{1-x}Mg_xO$ supercell structures that are permitted by the superior neutron scattering results. Figure 8 clearly shows the greatly enhanced data quality of the neutron scattering measurements, compared with x-ray experiments. The neutron data lead to better precision (see Table I and ref.[7]), as well as better accuracy, in the subsequent structure analyses.

It is also noteworthy that the structure modeling for the PDF or Rietveld analyses can confine the range of structural information that is sought. For example, Rietveld refinement of $Zn_{1-x}Mg_xO$ used only one positional parameter, and therefore MgO_4 and ZnO_4 tetrahedra are characterized by the same c/a and u. In the x-ray PDF refinement, two position parameters were refined, so that we could differentiate u(Mg) and u(Zn), but not their c/a ratios. However, for the neutron PDF refinement, we used four positional parameters as variables, and were able to distinguish the MgO_4 and ZnO_4 geometries through both c/a and u. Again, the choice of a structural model relies on the quality of the diffraction data, for this application on a system with relatively low-atomic-number elements. The neutron data showed sufficient integrity for testing various structure models, which were not possible for the x-ray data alone.

IV. CONCLUSION

Detailed structural analyses of $Zn_{1-x}Mg_xO$ ($0 \leqslant x \leqslant 0.15$) solid solutions, focusing on the dissimilar local geometries of Mg and Zn, have been performed by using Raman scattering, $^{67}Zn/^{25}Mg$ NMR spectroscopy, and neutron Rietveld/PDF analyses. Line broadenings of the Raman and $^{67}Zn/^{25}Mg$ NMR spectra imply that Mg-substitution into a

ZnO-rich lattice gradually increases the configurational disorder and crystal defects in the lattice. Rietveld refinement of time-of-flight neutron diffraction patterns and Raman peak profile analyses show that the macroscopic lattice distortions in $Zn_{1-x}Mg_xO$ wurtzites develop in a way such that the c/a ratio decreases with Mg content x. A real-space neutron PDF analysis using a supercell model of Zn_7MgO_8 reveals that the Mg and Zn atoms in $Zn_{1-x}Mg_xO$ have markedly distinct local geometries: MgO_4 tetrahedra are smaller in height and volume and have a larger internal parameter u. The wurtzite structural parameters c/a and u for MgO_4 deviate from their ideal values, in agreement with computational predictions of wurtzite MgO structures. Previous DFT studies on $Zn_{1-x}Mg_xO$ supercells and the present neutron PDF analysis strongly suggest that Mg-substitution will increase the spontaneous polarization of ZnO.

ACKNOWLEDGEMENTS

The authors acknowledge support from the National Science Foundation through the MRSEC program (DMR05-20415) and from the Department of Energy, Basic Energy Sciences, Catalysis Science Grant No. DE-FG02-03ER15467. This work has benefited from the use of NPDF at the Lujan Center at Los Alamos Neutron Science Center, funded by DOE Office of Basic Energy Sciences. Los Alamos National Laboratory is operated by Los Alamos National Security LLC under DOE Contract DE-AC52-06NA25396. The authors are grateful to the NSF-supported National High Magnetic Field Laboratory, in Tallahassee, Florida for access to the high-field (19.6 T) NMR facilities, and to Zhehong Gan for assistance with the NMR measurements. Andrei Malashevich and David Vanderbilt kindly provided the DFT optimized structural data for $Zn_{1-x}Mg_xO$ supercells. The authors also thank Brent Melot and Daniel Shoemaker for the neutron data collection.

[1] A. Tsukazaki, A. Ohtomo, T. Kita, Y. Ohno, H. Ohno, and M. Kawasaki, Science **315**, 1388 (2007).
[2] K. Koike, K. Hama, I. Nakashima, G. Takada, M. Ozaki, K. Ogata, S. Sasa, M. Inoue, and M. Yano, Jpn. J. Appl. Phys. **43**, L1372 (2004).
[3] S. Rajan, H. Xing, S. DenBaars, U. K. Mishra, and D. Jena, Appl. Phys. Lett. **84**, 1591 (2004).
[4] S. Sasa, M. Ozaki, K. Koike, M. Yano, M. Inoue, Appl. Phys. Lett. **89**, 053502 (2006).
[5] H. Tampo, H. Shibata, K. Matsubara, A. Yamada, P. Fons, S. Niki, M. Yamagata, and H. Kaine, Appl. Phys. Lett. **89**, 132113 (2006).
[6] J. H. Davies, *The Physics of Low-Dimensional Semiconductors: An Introduction* (Cambridge University Press, New York, 1998).
[7] Y.-I. Kim, K. Page, and R. Seshadri, Appl. Phys. Lett. **90**, 101904 (2007).
[8] Y.-I. Kim, K. Page, A. M. Limarga, D. R. Clarke, and R. Seshadri, Phys. Rev. B **76**, 115204 (2007).
[9] Th. Proffen, T. Egami, S. J. L. Billinge, A. K. Cheetham, D. Louca, and J. B. Parise, App. Phys. A **74**, S163 (2002).
[10] D. A. Shirley, Phys. Rev. B **5**, 4709 (1972).
[11] P. Thompson, D. E. Cox, and J. B. Hastings, J. Appl. Cryst. **20**, 79 (1987).
[12] M. Yoshikawa, Mater. Sci. Forum. **52-53**, 365 (1989).
[13] R. Dupree and M. E. Smith, J. Chem. Soc. Chem. Commun. **1988**, 1483.
[14] D. Massiot, F. Fayon, M. Capron, I. King, S. Le Calve, B. Alonso, J.-O. Durand, B. Bujoli, Z. Gan, and G. Hoatson, Mag. Reson. Chem. **40**, 70 (2002).
[15] P. F. Peterson, M. Gutmann, Th. Proffen, and S. J. L. Billinge, J. Appl. Cryst. **32**, 1192 (2000).
[16] C. L. Farrow, P. Juhas, J. W. Liu, D. Bryndin, E. S. Bozin, J. Bloch, Th. Proffen, and S. J. L. Billinge, J. Phys.:Condens. Matter **19**, 335219 (2007).
[17] A. C. Larson and R. B. von Dreele, Los Alamos National Laboratory Report No. LAUR 86-748, 1994.
[18] B. H. Toby, J. Appl. Cryst. **34**, 210 (2001).
[19] J. M. Calleja and M. Cardona, Phys. Rev. B **16**, 3753 (1977)
[20] T. C. Damen, S. P. S. Porto, and B. Tell, Phys. Rev. **142**, 570 (1966).
[21] J. M. Zhang, T. Ruf, M. Cardona, O. Ambacher, M. Stutzmann, J.-M. Wagner, and F. Bechstedt, Phys. Rev. B **56**, 14399 (1997).
[22] H.-M. Cheng, K.-F. Lin, H.-C. Hsu, C.-J. Lin, L.-J. Lin, and W.-F. Hsieh J. Phys. Chem. B **109**, 18385 (2005).
[23] E. Kundla, A. Samoson, and E. Lippmaa, Chem. Phys. Lett. **83**, 229 (1981).
[24] E. S. Toberer, J. D. Epping, B. F. Chmelka, R. Seshadri, Chem. Mater. **18**, 6345 (2006)
[25] K. J. D. MacKenzie and R. H. Meinhold, Am. Miner. **79**, 250 (1994). Mg survey
[26] K. J. D. MacKenzie and R. H. Meinhold, Thermochim. Acta **230**, 331 (1993).
[27] M. Magi, E. Lippmaa, A. Samoson, G. Engelhardt, and A.-R. Grimmer, J. Phys. Chem. **88**, 1518 (1984).
[28] H. Sawada, R. Wang, and A. W. Sleight, J. Solid State Chem. **122**, 148 (1996).
[29] T. M. Sabine and S. Hogg, Acta Crystallogr. B **25**, 2254 (1969).
[30] S. C. Abrahams and J. L. Bernstein, Acta Crystallogr. B **25**, 1233 (1969).
[31] P. Harrison, G. A. Jeffrey, and J. R. Townsend, Acta Crystallogr. **11**, 552 (1958).
[32] J. Albertsson, S. C. Abrahams, and A. Kvick, Acta Crystallogr. B **45**, 34 (1989).
[33] E. H. Kisi and M. M. Elcombe, Acta Crystallogr. C **45**, 1867 (1989).
[34] V. F. Sears, Neutron News **3**, 26 (1992).
[35] I. D. Brown, *The Chemical Bond in Inorganic Chemistry: The Bond Valence Model* (Oxford University Press, Oxford, 2002).
[36] I. D. Brown, Acta Crystallogr. B **48**, 553 (1992).
[37] Y.-I. Kim and R. Seshadri, J. Korean Phys. Soc. in press.
[38] Y.-I. Kim and R. Seshadri, Inorg. Chem. in press.

[39] N. E. Brese and M. O'Keeffe, Acta Crystallogr. B **47**, 192 (1991).
[40] R. D. Shannon, Acta Crystallogr. A **32**, 751 (1976).
[41] S. Limpijumnong and W. R. L. Lambrecht, Phys. Rev. B **63**, 104103 (2001).
[42] A. Janotti, D. Segev, and C. G. Van de Walle, Phys. Rev. B **74**, 045202 (2006).
[43] P. Gopal and N. A. Spaldin, J. Electron. Mater. **35**, 538 (2006).
[44] A. Malashevich and D. Vanderbilt, Phys. Rev. B **75**, 045106 (2007).
[45] X. F. Fan, H. D. Sun, Z. X. Shen, J.-L. Kuo, and Y. M. Lu, J. Phys.:Condens. Matter **20**, 235221 (2008).
[46] A. Malashevich and D. Vanderbilt, private communications.
[47] A. Dal Corso, M. Posternak, R. Resta, and A. Baldereschi, Phys. Rev. B **50**, 10715 (1994).
[48] F. Bernardini, V. Fiorentini, and D. Vanderbilt, Phys. Rev. B **56**, R10024 (1997).
[49] Y. Noel, C. M. Zicovich-Wilson, B. Civalleri, Ph. D'Arco, and R. Dovesi, Phys. Rev. B **65**, 014111 (2001).

APPENDIX

Complete list of atomic coordinates for the 16-atom wurtzite supercell Zn_7MgO_8 ($a = b = 6.5054$ Å, $c = 5.2015$ Å, $\alpha = \beta = 90°$, $\gamma = 120°$), as determined by the neutron PDF analysis.

Atom	x	y	z	Type
Zn	0.1667	0.3333	0	Zn1
	0.6667	0.3333	0	Zn3
	0.1667	0.8333	0	Zn1
	0.6667	0.8333	0	Zn1
	0.3333	0.1667	0.5	Zn2
	0.8333	0.1667	0.5	Zn2
	0.8333	0.6667	0.5	Zn2
Mg	0.3333	0.6667	0.486(8)	Mg
O	0.1667	0.3333	0.386(3)	O2
	0.6667	0.3333	0.3825(8)	O3
	0.1667	0.8333	0.386(3)	O2
	0.6667	0.8333	0.386(3)	O2
	0.3333	0.1667	0.8825(8)	O3
	0.8333	0.1667	0.8825(8)	O3
	0.3333	0.6667	0.858(5)	O1
	0.8333	0.6667	0.8825(8)	O3